

Earthquake clustering and stress inversion in the Mendocino Triple Junction region

Yu-Fang Hsu,¹ Patricia Martínez-Garzón,^{2,3} Daniel T. Trugman⁴ and Yehuda Ben-Zion^{1,5}

¹Department of Earth Sciences, University of Southern California, Los Angeles, 90089, USA. E-mail: yufanghs@usc.edu

²GFZ Helmholtz Centre for Geosciences, Potsdam, 14473, Germany

³RWTH University of Aachen, Aachen, 52062, Germany

⁴Nevada Seismological Laboratory, University of Nevada, Reno, 89557, USA

⁵Statewide California Earthquake Center, University of Southern California, Los Angeles, 90089, USA

Accepted 2026 February 26. Received 2026 January 22; in original form 2025 October 16

SUMMARY

The Mendocino Triple Junction (MTJ), where the Gorda, North American and Pacific plates meet, is one of the most seismically active regions in California. The tectonic movements along the Mendocino transform fault zone (MTFZ), Gorda slab (GS) and northern San Andreas Fault systems (NSAF) lead to high background seismicity rates but relatively low aftershock productivity. To improve the understanding of earthquake processes in the area, we analyse relations between background seismicity, aftershock productivity and stress parameters. We apply the nearest-neighbour approach to investigate the spatial distributions and properties of background and clustered seismicity, and invert focal mechanisms of events in Voronoi cells for features of the deviatoric stress field. The results indicate that the intensity of background seismicity and aftershock productivity decrease with distance from the MTJ, defined here for simplicity as the hypocentre of the 1992 M_w 7.2 main shock. We also find that the stress regime is the most compressive in the area directly surrounding the MTJ. In the MTFZ and GS, the compressive stress decreases with increasing distance from the MTJ, correlating with the reduced aftershock productivity and background seismicity. In the NSAF, the observed relations between the stress, aftershock productivity and background seismicity are not clear, possibly due to crustal extension related to the slab window and elevated heat flow. Compared to the MTFZ and GS, the NSAF has a higher foreshock proportion, lower aftershock proportion and small-to-medium main shock magnitudes, indicating more swarm-like clusters in this region. The inverted stress regimes in the MTFZ and NSAF are dominated by strike-slip faulting. The GS exhibits mostly strike-slip and normal mechanisms despite the subduction environment, which may reflect slab bending and reactivation of pre-existing normal faults.

Key words: Seismicity and tectonics; Statistical seismology; Dynamics: seismotectonics.

1 INTRODUCTION

Distinguishing background seismicity from clustered seismicity and identification of earthquake clusters can provide important insights into earthquake triggering processes and sequence evolution (I. Zaliapin & Y. Ben-Zion 2013a, b). The proportion of background versus clustered events has been observed to depend on several factors, including aspects of the stress field and its heterogeneities (N. Abolfathian *et al.* 2018; P. Martínez-Garzón *et al.* 2018; T.H. Goebel *et al.* 2019) and the presence of fluids and heat flow (I. Zaliapin & Y. Ben-Zion 2016a, b; D.T. Trugman & Y. Ben-Zion 2023). Despite previous analyses in selected regions and environments, a quantitative characterization of earthquake clustering and the stress field in a complex triple junction region can provide useful insights. How are features of the stress field correlated with clustering of the seismicity, including the productivity of aftershock sequences and the occurrence of foreshocks?

Cape Mendocino is one of the most seismically active regions in California and hosts the intersection of the Cascadia subduction zone, the Mendocino Transform Fault and the northern part of the San Andreas Fault. These different tectonic structures meet in the Mendocino Triple Junction (MTJ) and produce a spatially heterogeneous stress field and complex seismicity patterns, making the region a natural laboratory to understand clustering processes. In the past 40 yr, three $M_w \geq 7$ earthquakes and more than 10 $M_w \geq 6$ earthquakes have occurred in this region, which includes oceanic and continental transform faults as well as a subduction slab. The combined deformation of these tectonic structures makes the earthquake rate in the Cape Mendocino region one of the highest in California and results in complex seismic and aseismic processes (K. Materna *et al.* 2018; D.R. Shelly *et al.* 2024). Interestingly, despite

the high seismicity rate, the aftershock productivity of earthquake clusters in Cape Mendocino is the lowest in the Western US (J.L. Hardebeck *et al.* 2019; D.T. Trugman & Y. Ben-Zion 2023).

The MTJ hosts a transition from transform to subduction motion, resulting in pronounced variations in deformation behaviours and tectonic settings. The Gorda Ridge spreads and the Gorda plate subducts in Cape Mendocino beneath the North American Plate (NAP) at a rate of 2–3 cm yr⁻¹ in the direction of N50°–55°E, forming the Cascadia subduction zone and its associated megathrust systems (R. Riddihough 1984). The Gorda Plate moves relative to the Pacific Plate at a rate of 5 cm yr⁻¹ in the direction of N115°E, leading to the right-lateral Mendocino Transform Fault at the boundary (R. Riddihough 1984). A slab window is formed at the southern edge of the Gorda plate due to the tectonic transition from subduction to translation motion (W.R. Dickinson & W.S. Snyder 1979; K.P. Furlong *et al.* 1989).

Consistent with the complex tectonic settings, the main shocks in the Cape Mendocino exhibit diverse faulting types, reflecting a heterogeneous stress field. The 1992 M_w 7.2 main shock was a reverse faulting event occurring at the overriding NAP, and it dynamically triggered two large right-lateral strike-slip aftershocks at the Gorda Slab with M_w of 6.5 and 6.6 (D. Oppenheimer *et al.* 1993; M.T. Hagerty & S.Y. Schwartz 1996; H. Guo *et al.* 2021). In 2021 and 2022, two $M_w > 6$ strike-slip events occurred in the Mendocino Transform Fault and Gorda Slab, respectively (W.L. Yeck *et al.* 2023). More recently, the 2024 M_w 7.0 main shock associated with strike-slip faulting occurred in the Mendocino Transform Fault (C.E. Yoon & D.R. Shelly 2024; F.F. Pollitz *et al.* 2025; M. Hellweg *et al.* 2025; J. Atterholt *et al.* 2025).

Previous studies have shown that aftershock productivity varies systematically with faulting types, fault complexity, heat flow and tectonic settings (K. Dascher-Cousineau *et al.* 2020; D.T. Trugman & Y. Ben-Zion 2023). The diverse stress regimes and tectonic settings in the Cape Mendocino area, together with anomalously low aftershock productivity, raises fundamental questions about the physical controls on earthquake clustering across complex plate boundaries. In this paper, we analyse properties of seismicity clusters and the stress field in the Cape Mendocino area, and explore how background seismicity, aftershock productivity and stress parameters vary internally in this tectonically complex region.

To examine the influence of different tectonic structures on clustering and stress features, we separate our study area into three tectonic groupings based on the dominant tectonic structures (Fig. 1): the Gorda Slab (GS), the Mendocino Transform Fault Zone (MTFZ) and the northern San Andreas Fault system (NSAF). The GS includes events in the subduction slab with depths of >20 km (K.P. Furlong *et al.* 2024). The MTFZ region contains earthquakes above the GS with depths of <20 km, including events in the Mendocino Transform Fault proper, the uppermost Gorda Plate and the continental crust part of the MTJ. The NSAF contains events south of the slab edge with latitudes in the range of 38.5°–40°, including the seismicity along the San Andreas Fault, Maacama Fault and Bartlett Springs Fault systems. Each group may include multiple faults and accommodate mixed styles of deformation, and the group names are used to indicate major tectonic structure rather than implying that all earthquakes occur on a single named fault.

We apply the nearest-neighbour approach (I. Zaliapin & Y. Ben-Zion 2013a, 2016a) to investigate characteristics of background and clustered seismicity in the study area, and invert earthquake focal mechanisms for stress field parameters with the MSATSI algorithm in these three subregions (P. Martínez-Garzón *et al.* 2014, 2016). These analyses provide important insights into how the various processes in the MTJ area affect the spatial variations of earthquakes and stress parameters, and in particular, the decay of aftershock productivity, background seismicity and the stress level with distance from the triple junction. The observed spatial correlations provide a framework for understanding key seismicity parameters and crustal stress heterogeneity in other triple-junctions and complex tectonic settings globally.

2 DATA AND METHODS

In the following subsections, we first describe the data selection for analysis of earthquake clusters using the nearest-neighbour approach. Then we introduce the focal mechanism catalogue, group discretization of focal mechanisms and the stress inversion method.

2.1 Identification of earthquake clusters

2.1.1 Earthquake catalogue

We use the waveform-relocated earthquake catalogue published by the Northern California Earthquake Data Center (see Data and Resources) from 1984 January 1 to 2025 January 31 for earthquake clustering analysis. The study area ranges from –126.5° to –122.9° in longitude and 38.5° to 42° in latitude. This catalogue has the lowest location errors and the most complete long-term data around the Mendocino Triple Junction area. The catalogue uses arrival time detections from the Northern California Seismic Network and improves the event location with waveform cross-correlation and double-difference (DD) methods (F. Waldhauser & W.L. Ellsworth 2000; F. Waldhauser 2001). The average absolute location errors are 0.17 km horizontally and 0.26 km vertically, while the average DD relative location errors are 0.45 km horizontally and 0.29 km vertically (F. Waldhauser & D.P. Schaff 2008). Since this catalogue includes various types of magnitudes, we homogenize them for the subsequent analysis into potency magnitude (M_p) based on the empirical magnitude conversion relations of D.T. Trugman & Y. Ben-Zion (2024). The potency magnitude is similar to moment magnitude but

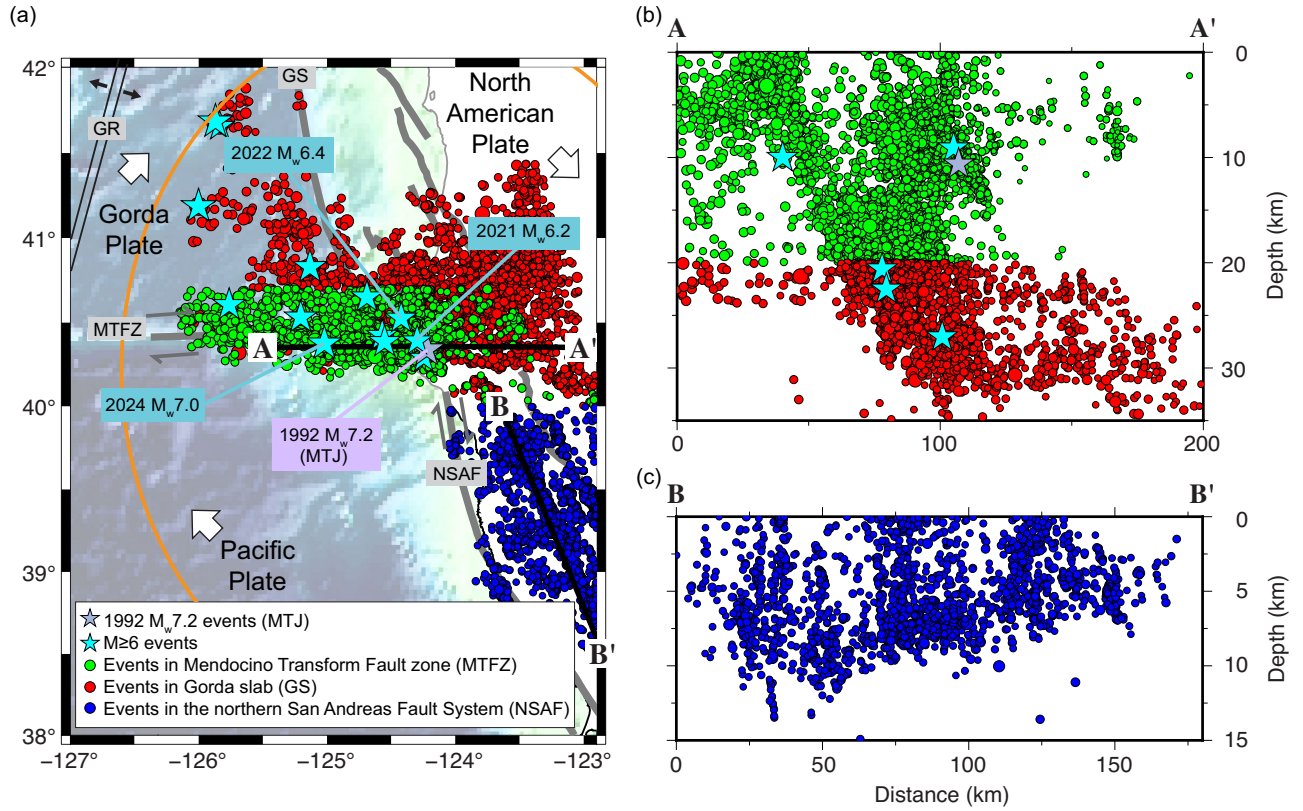


Figure 1. (a) Tectonic setting in Cape Mendocino together with instrumental seismicity with $M_p \geq 2.5$ between 1984 January 1 and 2025 January 31. The dots represent the seismic events categorized by tectonic regions: the Mendocino Transform Fault Zone (MTFZ), the Gorda Slab (GS) and the Northern San Andreas Fault system (NSAF). The location of the Mendocino Triple Junction (MTJ) is defined as the hypocentre of the 1992 M_w 7.2 main shock. The abbreviation of GR denotes the Gorda Ridge. Arrows indicate the sense of plate motion. The thick and thin lines are faults and coastlines. The highlighted circular area includes the events used for aftershock productivity analysis in Fig. 5, Figs S1 and S9. (b) Depth distribution of events along the A–A’ profile. The stars in (a) and (b) mark $M_w \geq 6$ earthquakes. Events located within ~ 15 km from the profile line are projected onto the profile. (c) Depth distribution of events along the B–B’ profile.

does not include an assumed rigidity at the earthquake source, which does not affect the seismic radiation to the bulk and is also not well defined (e.g. Y. Ben-Zion 2001).

The magnitude of completeness in the study area has space–time variations but is generally around 2. I. Zaliapin & Y. Ben-Zion (2015) showed that location errors larger than the estimated rupture length produce artefacts in analysis using the nearest-neighbour approach. To minimize such artefacts, we use in the analysis only events with rupture lengths larger than the mean absolute horizontal location errors, which corresponds to potency magnitudes of $M_p \geq 2.5$. The rupture length of each earthquake is estimated from its potency value assuming a circular crack (appropriate for small events for which location errors may have significant effects) and a strain drop of 10^{-4} , equivalent to a stress drop of 3 MPa assuming a nominal rigidity of 30 GPa (Y. Ben-Zion 2008).

2.1.2 Nearest-neighbour analysis

The nearest-neighbour analysis provides a data-driven approach for identifying earthquake clusters, separating seismicity into background and clustered modes, and declustering seismic catalogues (e.g. M. Baiesi & M. Paczuski 2004; I. Zaliapin & Y. Ben-Zion 2013a, 2020; P. Martínez-Garzón *et al.* 2019; S. Gentili *et al.* 2019; K. Karimi & J. Davidsen 2023; Y.F. Hsu *et al.* 2024). This method identifies for each earthquake an earlier nearest-neighbour event with the closest proximity in the combined space and time domains. To find the nearest neighbour of event j , we calculate the earthquake proximity η_{ij} between event j and each event i occurring earlier using

$$\eta_{ij} = \begin{cases} t_{ij}^d r_{ij}^{d-bm_i} 10^{-bm_i} & \text{if } t_{ij} > 0 \\ \infty & \text{if } t_{ij} \leq 0 \end{cases}, \quad (1)$$

where $t_{ij} = t_j - t_i$ is the temporal distance (in yr) between event pair (i, j) , r_{ij} is the 2-D or 3-D spatial distance (in km) between event pair (i, j) , d is the fractal dimension of epicentres or hypocentres, b is the b -value of the Gutenberg–Richter statistics in the research area and m_i is the magnitude of event i . In this study, we calculate earthquake proximity η_{ij} with 3-D distances between hypocentres of event pairs with parameters $d = 2.6$ and $b = 1$ (C. Sammis *et al.* 1987; I. Zaliapin & Y. Ben-Zion 2013a). In the event pair (i, j) , event j

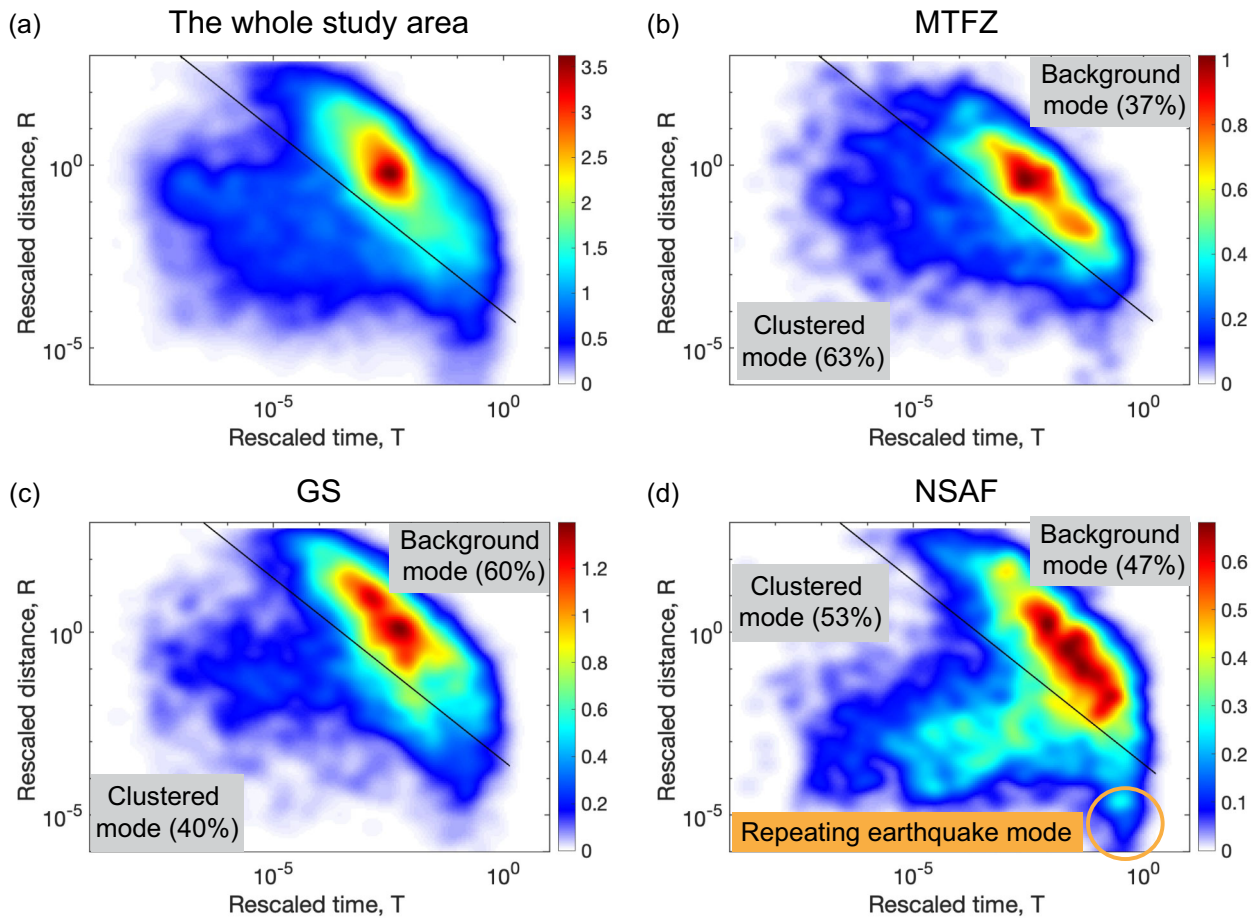


Figure 2. The joint distribution of rescaled time (T) and space (R) components of the nearest-neighbour proximity (eq. 2) of $M_p \geq 2.5$ events from 1984 January 1 to 2025 January 31 in the F. Waldhauser & D.P. Schaff (2008) catalogue in (a) the whole study area, (b) MTFZ, (c) GS and (d) NSAF. The line in (a) is $\log T + \log R = -4.03$. The scalebar is the kernel density of the event distribution.

is referred to as an offspring of a parent defined as the nearest-neighbour event i , which is the earthquake with minimum earthquake proximity given by eq. (1). The nearest-neighbour proximity η_{ij} can be represented as a product of its rescaled spatial distance R_{ij} and rescaled time distance T_{ij} :

$$\eta_{ij} = T_{ij}R_{ij} \quad (2)$$

$$T_{ij} = t_{ij}10^{-pbm_i}; R_{ij} = r_{ij}^d10^{-(1-p)bm_i} \quad (3)$$

Here we use $p = 0.5$ following I. Zaliapin & Y. Ben-Zion (2013a, 2013b, 2016a).

The joint distribution (T , R) typically exhibits a bimodal distribution, consisting of background and clustered modes (Fig. 2). The diagonal line in Fig. 2 characterizes a time-stationary Poisson process characterized by $\log T + \log R = \text{const}$. The mode along and above the diagonal line corresponds to background seismicity with nearest neighbours following a Poissonian process. In contrast, the mode below the diagonal line represents clustered seismicity with smaller proximities compared to a random distribution. To differentiate between background seismicity and earthquake clusters, we construct a time-oriented spanning tree by connecting each offspring to its parent and removing links between parents and offspring with a threshold $\eta_{ij} > \eta_0$ typical for a random distribution (I. Zaliapin & Y. Ben-Zion 2013a). The threshold η_0 is estimated by the Gaussian mixture model based on the log η -distribution of event pairs (I. Zaliapin & Y. Ben-Zion 2016a). This separation divides the spanning tree into a collection of individual trees, each representing an earthquake cluster. In each cluster, we define the event with the largest magnitude as the main shock, and events occurring before and after the main shock as foreshocks and aftershocks, respectively. In the MTJ study area (Fig. 1), 46 per cent and 54 per cent of the events are identified as background and clustered seismicity, respectively (Fig. 2). The relatively low fraction of clustered events is consistent with the low aftershock productivity found earlier (D.T. Trugman & Y. Ben-Zion 2023).

2.1.3 Aftershock productivity

To have a robust assessment of the aftershock productivity of earthquake clusters with different main shock magnitudes, we calculate Δ -aftershocks to equalize the magnitude range of aftershocks in each cluster. We choose main shocks with $M \geq \Delta + 2.5$ and aftershocks with Δ below their corresponding main shock magnitude (i.e. Δ -aftershocks) for analysis. To evaluate the robustness of the results, we further examine the sensitivity of aftershock productivity to variations in $\Delta = 2, 3$ and 3.5 for the GS and MTFZ (Fig. S1). For the NSAF region with relatively small main shock magnitudes, we use for the analysis $\Delta = 1.5$.

2.2 Stress analysis

The stress field plays a key role in earthquake dynamics and can impact the cluster patterns in space and time. Following A.J. Michael (1987) and later works, a diverse population of earthquake focal mechanisms can be inverted for the remote tectonic stress field that is most likely to produce that event population. Since a large fraction of the seismicity is part of earthquake clusters triggered locally by previous events (I. Zaliapin & Y. Ben-Zion 2022), rather than by the remote tectonic loading, inversions for the remote background stress field should use background (declustered) earthquakes (P. Martínez-Garzón *et al.* 2016). Most stress inversion studies use entire catalogues rather than declustered events, although in such cases the interpretation of the derived stress field is less clear. In this study, we invert focal mechanisms of background seismicity to examine aspects of the tectonic stress field in different parts of the Mendocino area. For comparison, we also invert mechanisms in the entire catalogue.

We utilize the focal mechanism catalogue provided by the Northern California Earthquake Data Center (C.P. NCEDC 2014) to invert for the deviatoric stress states of background and the entire seismicity. This focal mechanism algorithm determines double couple fault plane solutions by minimizing first-motion polarity discrepancies for each event (P. Reasenber & D. Oppenheimer 1986). The background seismicity is obtained from the catalogue using the declustering algorithm of I. Zaliapin & Y. Ben-Zion (2020). Following the earthquake clustering analysis, we use 2635 background and 5205 all focal mechanisms in Cape Mendocino, maintaining the same minimum M_p , space and time domain as the seismic catalogue for stress inversion analysis. The median values of the maximum half-width of 90 per cent confidence range for strike, dip and rake in Cape Mendocino are 15° , 23° and 30° , respectively.

2.2.1 Discretization of focal mechanism groups

Appropriate discretization of focal mechanism groups is important for robust stress inversion results. During the stress inversion, improper seismicity discretization can lead to potential artefacts in the inverted stress orientations and biased physical interpretations of the local stress field (e.g. J.L. Hardebeck & E. Hauksson 1999; J. Townend & M.D. Zoback 2001; J.L. Hardebeck & A.J. Michael 2004). To improve the robustness of stress orientations, we apply the k-means optimization grouping algorithm to discretize focal mechanism groups according to their spatial distribution (J.A. Hartigan & M.A. Wong 1979; P. Martínez-Garzón *et al.* 2016). The number of groups is determined by iteration of the k-means grouping algorithm. In each iteration, every focal mechanism is assigned to the group with the nearest centroid, minimizing a squared error function (J)

$$J = \sum_{j=1}^k \sum_{i=1}^n |x_i^{(j)} - c_j|^2, \quad (4)$$

where x is the location of the earthquake i and c is the location of the j -nearest group centroid. We use Cartesian squared Euclidean distances between event hypocentres and group centroids to optimize clustering. The spatial extent of the grid cells for the focal mechanism groups is defined by a centroidal Voronoi tessellation (G. Voronoi 1908). In this study, we separate the focal mechanisms of background and all seismicity into 40 and 71 groups, respectively. Every group contains a minimum of 40 focal mechanisms.

2.2.2 Stress inversion

The stress inversion has three main assumptions: (i) the stress field is homogeneous within a given space–time domain, (ii) earthquakes are distributed on pre-existing faults with different orientations and (iii) the fault slip follows the direction of maximum shear traction (R.E. Wallace 1951; M.H. Bott 1959). We use the refined MSATSI linear damped stress inversion technique to investigate the characteristics of stress fields in Cape Mendocino since this technique can mitigate the artefacts resulting from focal mechanism discretization (J.L. Hardebeck & A.J. Michael 2006; P. Martínez-Garzón *et al.* 2014; 2016). This algorithm iteratively performs stress inversion to determine the nodal planes optimally oriented for failure according to an instability coefficient I (V. Vavryčuk 2011, 2014; P. Martínez-Garzón *et al.* 2016). The coefficient I quantifies how close a given fault orientation is to failure under given shear stress (τ), normal stresses (σ_n) and friction coefficient (μ)

$$I = \frac{\tau - \mu (\sigma_n - \sigma_1)}{\tau_{\text{opt}} - \mu (\sigma_{\text{opt}} - \sigma_1)}, \quad (5)$$

where τ_{opt} and σ_{opt} are the shear and normal stress components of optimally oriented faults, respectively (V. Vavryčuk 2011; V. Vavryčuk *et al.* 2013). The value μ varies from 0.2 to 0.8 and is determined through iterative computations during the stress inversion process. The instability coefficient (I) varies from 0 to 1. The values $I = 0$ and $I = 1$ indicate the faults least and most favourably oriented to fail under a given deviatoric stress field, respectively. In each iteration, the nodal plane with the largest I in each focal mechanism is selected for the next iteration. Uncertainties of fault plane orientations are estimated by 20 bootstrap resamplings of focal mechanisms (A.J. Michael 1987; J.L. Hardebeck & A.J. Michael 2006). The following sections describe details of the inverted stress field, including maximum horizontal stress orientations (S_{HMax}), stress ratio (R -value) and A_ϕ parameters.

Maximum horizontal stress orientations (S_{HMax}): We compute orientations of three principal stress axes based on the algorithm of B. Lund & J. Townend (2007) and classify the estimated trends and plunges of the principal stresses into normal, reverse, strike-slip and oblique faulting according to the classification proposed by M.L. Zoback (1992), which is based on the relative orientation of the P, T and B axes.

Stress ratio: The stress ratio parameter (R -value) describes the relative magnitudes of the three principal stresses on fault planes, which is defined as

$$R = (\sigma_1 - \sigma_2) / (\sigma_1 - \sigma_3), \quad (6)$$

where σ_1 , σ_2 , σ_3 represent the most, intermediate and least compressive principal stresses. The value of R ranges from 0 to 1. If σ_1 is close to σ_2 in size, $R \approx 0$. If σ_2 is similar to σ_3 in size, $R \approx 1$. In a strike-slip environment, $R \approx 0$ and $R \approx 1$ indicate transtensional and transpressional regimes, respectively. In a reverse faulting region, $R \approx 0$ and $R \approx 1$ indicate radial reverse faulting and a mixture of reverse and strike-slip faulting, respectively.

A_ϕ parameter: We further use the A_ϕ parameter to describe the relative stress magnitude of each focal mechanism group combining the relative size of the three principal stresses and fault regimes:

$$A_\phi = (n + 0.5) + (-1)^n (0.5 - R), \quad (7)$$

where R is the stress ratio of each focal mechanism group, and n is the index number for fault regimes with $n = 0, 1, 2$ representing normal faulting, strike-slip faulting and reverse faulting, respectively (R.W. Simpson 1997; J.E. Lundstern 2024). The A_ϕ parameter ranges from 0 to 3. Larger A_ϕ values suggest higher compressive stresses. The values $A_\phi = 0$ and $A_\phi = 3$ indicate radial normal and radial reverse faulting with isotropic horizontal principal stresses, respectively (J.E. Lundstern 2024).

3 RESULTS

3.1 Clustering analysis

Both background and clustered seismicity modes in the Cape Mendocino area exhibit their highest event intensities near the MTJ (Fig. 3). To the northeast of the GS, the background event intensity is generally higher than that of the clustered seismicity. The background event intensity in the SAF is much smaller than in the subparallel fault systems (e.g. the Maacama and Bartlett Springs faults), indicating that the SAF seismicity rate in the examined time period is very low. In addition, the GS exhibits the highest proportion of background seismicity (60 per cent) compared to the MTFZ (37 per cent), and NSAF (47 per cent) (Fig. 2). Fig. 4 shows the percentage of main shocks, foreshocks and aftershocks in the three subregions. The results indicate that the MTFZ has the highest percentage of aftershocks (78 per cent) but the lowest percentage of main shocks (12 per cent) and foreshocks (10 per cent) among our three analysed regions. The clusters in the overriding NAP contribute to the high aftershock proportion in MTF. An alternative event grouping assigns seismicity within the NAP above the subducting Gorda slab to the NAP rather than to the MTFZ (Fig. S2). In this classification, the NAP has the strongest clustered mode in the nearest-neighbour diagrams compared to the GS and MTFZ (Fig. S3). However, the foreshock fraction in the MTFZ is still the lowest, even though a set of events moved from the MTFZ to the NAP (Fig. S4). This is different from previous observations from the East Pacific Rise, where oceanic faults connecting mid-ocean ridges were observed to display almost one order of magnitude larger number of foreshocks than continental transform faults (J.J. McGuire *et al.* 2005).

The NSAF has the lowest percentage of aftershocks (55 per cent) but the highest percentage of main shocks (22 per cent) and foreshocks (23 per cent). The horizontal distribution of the clustered mode in the NSAF (Fig. 2d) is consistent with expectations for clusters of small-to-medium main shocks (Y.F. Hsu *et al.* 2024). Interestingly, the clustered mode in the NSAF is stronger than in other regions despite the smaller main shock magnitudes (Fig. 2). The high percentage of foreshocks and small main shock magnitudes in the NSAF suggest a partially aseismic driving process or more swarm-type activity than in the other two regions (X. Chen & P.M. Shearer 2013; I. Zaliapin & Y. Ben-Zion 2013b; Y.F. Hsu *et al.* 2024). We also observe a possible mode of repeating earthquakes in the NSAF (Fig. 2d), but it is less clear than what is found for the creeping section of the San Andreas fault (Y.F. Hsu *et al.* 2024) and the Marmara region of the North Anatolian Fault (P. Martínez-Garzón *et al.* 2019). The repeater mode in the NSAF is consistent with the observation of abundant repeating earthquakes and creeping behaviours along the Maacama Fault and the Bartlett Springs Fault (N. Shakibay Senobari & G.J. Funning 2019). In contrast, we do not identify a clear mode for repeaters in the MTFZ and GS (Fig. 2), even though previous studies have documented repeating earthquakes in this region (F. Waldhauser & D.P. Schaff 2008; K. Materna *et al.* 2018; F. Waldhauser & D.P. Schaff 2021). For the clear repeater mode with vertical distribution in the SAF, the repeating earthquakes exhibit

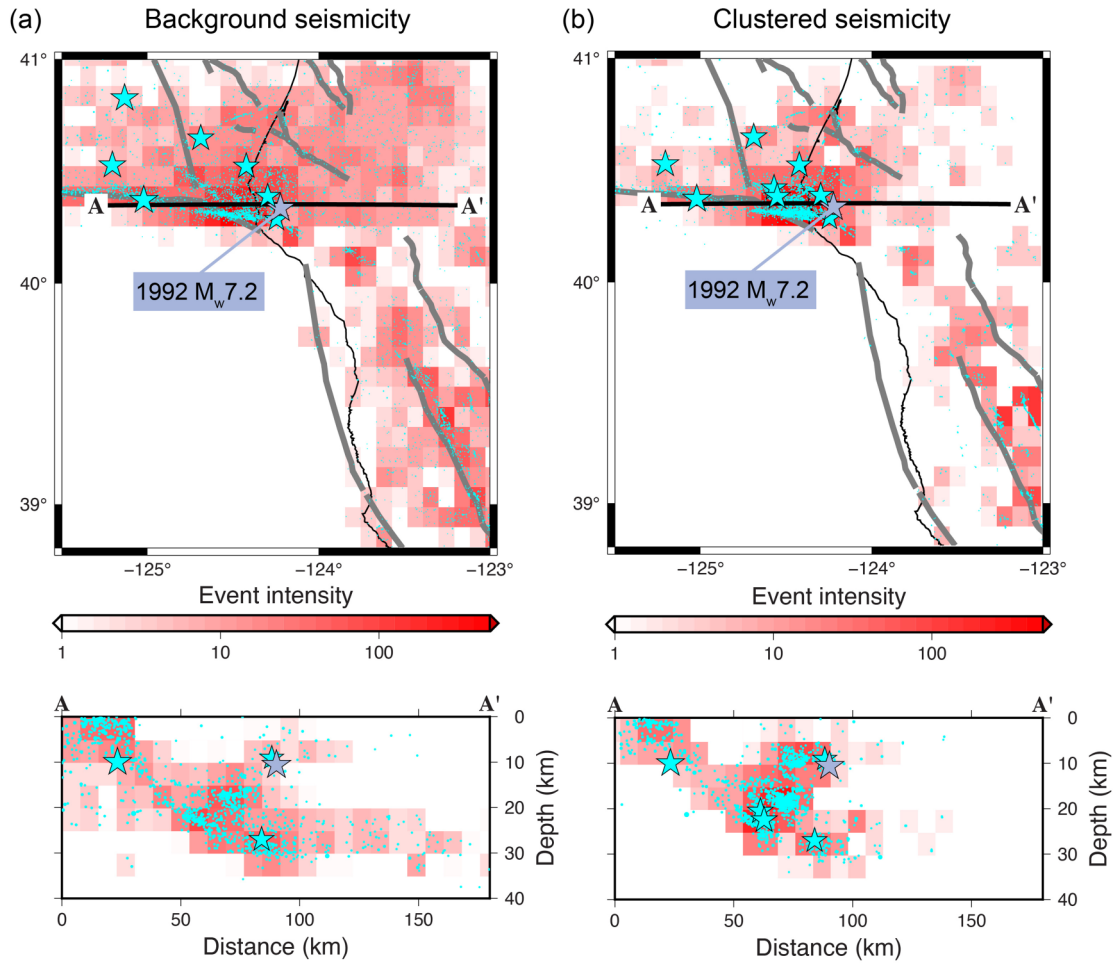


Figure 3. Distributions of background (a) and clustered (b) seismicity intensity (number of events per grid cell) in Cape Mendocino using a grid size of 10×10 km. The thick and thin lines mark faults and the coastline. The panels beneath the maps are the depth distribution of background and clustered seismicity along profile A–A' using a 10×5 km grid size. The stars in (a and b) show locations of $M_w \geq 6$ events between 1984 January 1 and 2025 January 31 and the dots show lower magnitude seismicity.

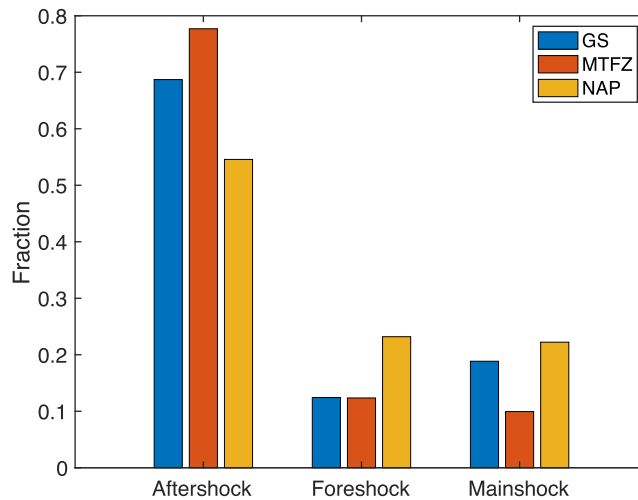


Figure 4. The proportion of aftershocks, main shocks, and foreshocks in the MTFZ, GS and NSAF.

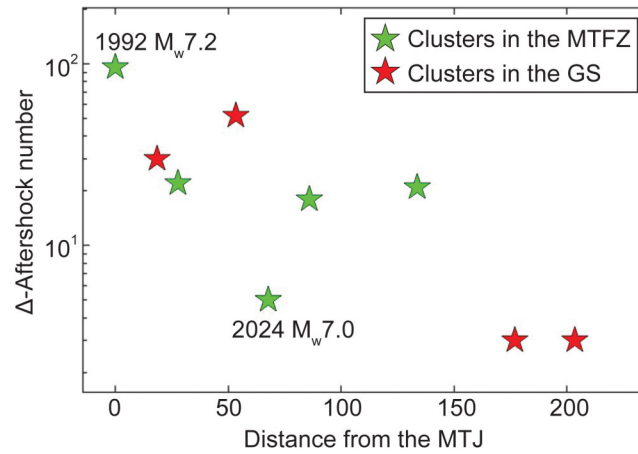


Figure 5. Relation between aftershock productivity of earthquake clusters in the MTFZ and GS and their main shock hypocentral distances (km) to the MTJ with $\Delta = 3.5$. The stars denote $M_w \geq 6$ main shocks. The MTJ location is defined as the hypocentre of the 1992 M_w 7.2 main shock.

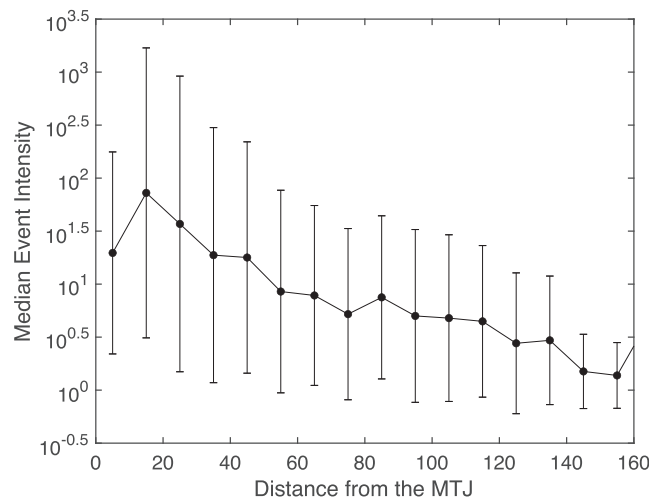


Figure 6. Median intensity of background seismicity in grid cells within the GS and MTFZ as a function of binned distance from the MTJ. The vertical lines denote error bars estimated by one standard deviation of event intensity of grids in the same bin.

relatively regular recurrence intervals that scale with the logarithm of seismic moment of parent events (Y.F. Hsu *et al.* 2024). The absence of the repeater mode in the MTJ suggests that repeating earthquakes there might exhibit more variable recurrence behaviour, or that repeating earthquakes are not enough to form a clear mode.

The logarithm of Δ -aftershock number of each cluster in the GS and MTFZ has a negative correlation with the hypocentral distance of their main shocks from the MTJ (Fig. 5). This can be seen for these regions using different Δ -values (Fig. S1), but is unclear for the NSAF. The decreasing aftershock productivity in the GS and MTFZ with distance from the MTJ is consistent with the notion that the stress level increases towards the triple junction (examined in the next section) and the expected correlation between aftershock productivity and the stress level (I. Zaliapin & Y. Ben-Zion 2016b). The background earthquake intensity in the GS and MTFZ also decreases with increasing distance from the MTJ (Fig. 6), while there are no clear trends between foreshocks and the distance from the MTJ (Fig. S5). The lower background event intensity within 0–10 km of the MTJ, compared to the 10–20 km distance, may reflect stress reduction during the 1992 M_w 7.2 main shock (Fig. 6), which may have suppressed subsequent background seismicity in the immediate vicinity of the fault. The intensity of foreshocks may be controlled by the temperature and fluid content in addition to the stress level (Y. Ben-Zion & V. Lyakhovskiy 2006; I. Zaliapin & Y. Ben-Zion 2013b, 2016b; D.T. Trugman & Y. Ben-Zion 2023).

3.2 Fault types

Figs 7(a) and (b) show the percentage of different faulting types of background and clustered seismicity derived from focal mechanism classification in the three subregions. Both types of seismicity in all subregions are dominated by strike-slip faulting. The background seismicity in the GS involves primarily the activation of strike-slip faults (48 per cent) and normal faults (35 per cent), even though the GS is part of a subduction zone (Fig. 7a). The predominant strike-slip and normal faulting reflect the flat subduction angle and reactivated normal faults from the spreading Gorda Ridge due to oblique subduction in the GS (S.P. Gulick *et al.* 2001). Although the

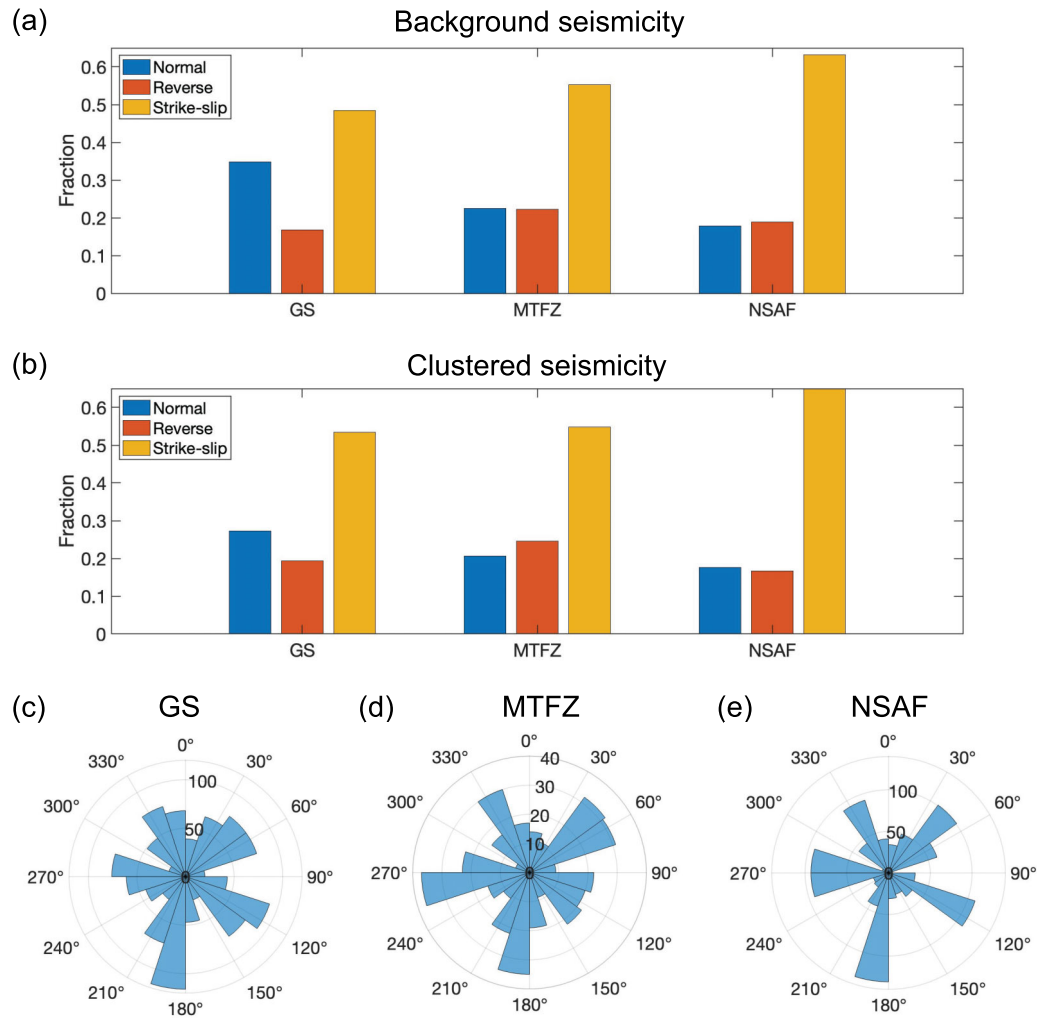


Figure 7. Proportion of focal mechanism type (normal, reverse and strike-slip faulting) of (a) background and (b) clustered seismicity in the GS, MTFZ and NSAF. (c–e) Strike distribution of background seismicity focal mechanisms in the GS, MTFZ and NSAF, respectively.

GS lies within a convergent setting, we observe higher background seismicity (60 per cent) together with a higher proportion of normal faulting compared to the NSAF and MTFZ (Fig. 7a).

The clustered seismicity in the GS exhibits a lower normal faulting (27 per cent) but a higher strike-slip fault percentage (53 per cent) compared to the background seismicity (Fig. 7b). The increasing percentage of strike-slip faults of clustered seismicity suggests that the stress perturbation of main shocks favours triggering aftershocks on strike-slip faults within the oceanic slab. The background seismicity in the MTFZ is dominated by strike-slip faults (55 per cent), which is comparable to that of clustered seismicity in the MTFZ (55 per cent). The background seismicity in the NSAF is also dominated by strike-slip faults (63 per cent) and is similar to that of clustered seismicity (66 per cent). The high strike-slip proportion in the MTFZ and NSAF (Fig. 7) for both background/clustered seismicity suggests that the stress patterns produced by the tectonic loadings and main shock stress transfers are similar in these regions. Under the alternative classification that defines the NAP as a separate group, the background seismicity within the NAP is dominated by strike-slip faulting (48 per cent) and reverse faulting (35 per cent) (Fig. S6). The stronger clustered mode and the higher fraction of reverse faulting in the NAP compared to the other regions suggest the relatively high compressive stress regime (Figs S2 and S6).

3.3 Stress regimes

The S_{HMax} orientation of background seismicity in the triple junction may be used to infer the directions of faults with optimal orientation for failure (Fig. 8a). The stress regime near the MTJ at a depth of ~ 10 km (around the hypocentre of the 1992 M_w 7.2 main shock) is characterized by reverse faulting with a northwest–southeast S_{HMax} orientation. In the GS, background seismicity shows predominantly north–south S_{HMax} orientations, and the stress regime of focal mechanism groups derived from the k-means method is a combination of strike-slip and normal faulting (Fig. 8a). The strike-slip faulting may be related to the pre-existing spreading ridge and its reactivated strike-slip faults (S.P. Gulick *et al.* 2001). The normal faulting of background seismicity is mostly located at the northeast,

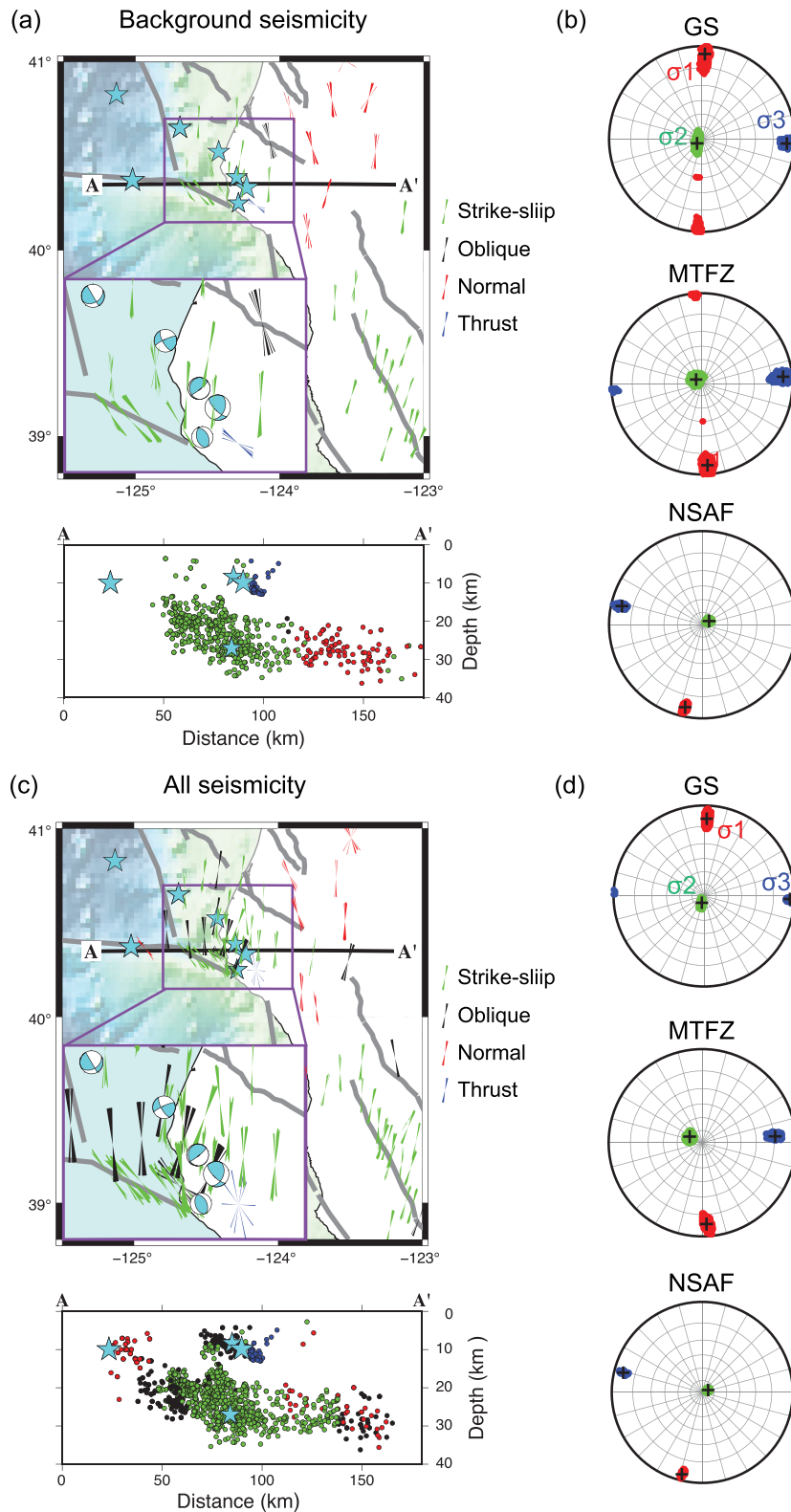


Figure 8. $S_{H_{max}}$ orientations of each Voronoi cell in Cape Mendocino based on the inversion of (a and b) background and (c and d) all seismicity. In (a) and (c), the thick and thin lines are faults and coastlines. The stars are $M_w \geq 6$ events between 1984 January 1, and 2025 January 31. The panels beneath the maps are the depth distribution of fault types in each Voronoi cell along profile A-A'. The classification of strike-slip, oblique, normal and thrust stress regimes are provided in the legend. (b and d) Stereonets based on the inversion of background and all seismicity in the GS, MTFZ and NSAF. The orientations of three principal stresses σ_1 , σ_2 , and σ_3 are provided in the plot, represented by the 95 per cent confidence interval from bootstrap resampling. The best orientation of each principal stress axis is given with a cross.

at greater downdip depths of the slab and the extended environment may result from the internal bending of the slab (Fig. 8a). In the north of the MTJ and GS, the S_{HMax} orientations of background seismicity are nearly parallel to the strike of the subduction margin (Fig. 8), reflecting oblique subduction of the GS beneath the NAP (T.J. Fitch 1972; K. Wang 2000). In the NSAF, the S_{HMax} orientations are about N20°E and form a consistent angle of 30°–40° with the Maacama and Bartlett Springs faults, suggesting that the NSAF is optimally oriented for failure assuming a friction coefficient of $\mu \approx 0.6$ (Fig. 8a).

Our derived S_{HMax} orientations based on the background seismicity are consistent with the orientation of the most compressive horizontal principal strain inverted from GPS velocity around the MTJ (Fig. S7; K.P. Furlong & R. Govers 1999; C.P. Nuyen & D.A. Schmidt 2022). In contrast, the most compressive horizontal principal strain rate with latitudes > 40.5° is northwest oriented, forming an angle of > 45° with the S_{HMax} orientation of background seismicity in the northeast GS (Fig. S7; C.P. Nuyen & D.A. Schmidt 2022). Although there is no physical requirement for GPS-derived strain rates to align with stress orientations inferred from focal mechanisms (K. Wang 2000), such alignment better fulfills stress inversion assumptions. The observed stress–strain misalignment in the GS does not contradict physical expectations, but suggests mechanical decoupling between land surface and subduction slab. Notably, the area with coordinates [–123.5, 40.5]° displays the smallest magnitude of compressive horizontal strain oriented E–W, and the stress field from focal mechanisms suggests a normal faulting style with the maximum horizontal stress oriented N–S (Fig. S7).

The S_{HMax} patterns of all seismicity are similar overall to those of background seismicity in the three subregions (Fig. 8), but show more variability that reflects the mixture of background seismicity and aftershocks (or more generally clustered events). At the MTJ, the S_{HMax} of all seismicity also lies $\sim 30^\circ$ from the structures around the longitude of 124.5°. North of the triple junction, the S_{HMax} implies nearly north–south compression, with stress regimes of focal mechanism groups dominated by strike-slip and oblique faulting (Fig. 8c). In the northeastern GS, S_{HMax} remains north–south-oriented with a regime of normal faulting. In the NSAF, the S_{HMax} is oriented 30°–40° from fault strikes, and the stress regime is dominated by strike-slip faulting (Fig. 8c).

The stereonets of the three principal stresses indicate that the average stress regime in these three subregions is strike-slip faulting (Figs 8b and d). Under the alternative classification which defines the NAP as a separate group, the NAP also exhibits a strike-slip regime (Figs S8b and S8d). The three principal stress orientations and plunges in the GS are generally consistent with the results of D. Li *et al.* (2018) (Fig. 8b). However, there is a notable discrepancy in the NAP. D. Li *et al.* (2018) report a reverse-faulting regime with σ_1 , σ_2 and σ_3 plunges of about 22°, 16° and 60°, whereas our results show a strike-slip regime with σ_1 , σ_2 and σ_3 plunges of 3°, 56° and 33° in the NAP (Figs S8b and S8d). Despite the difference in plunges, both studies identify similar horizontal stress orientations. This discrepancy may result from differences in the time span of the catalogue. D. Li *et al.* (2018) used data from 1980 to 2016, whereas our study includes events from January 1984 to 2025. The more recent strike-slip main shocks included in our data set may influence the stress inversion results and contribute to the differences in principal stress plunges.

The A_ϕ value of background seismicity is the highest at a depth of ~ 10 km in the MTJ with a stress regime characterized by thrust faulting (Fig. 9a), which indicates that this area has the most compressive stress level. The A_ϕ value of background seismicity in the oceanic slab beneath the MTJ area indicates a strike-slip faulting stress regime (Fig. 9a), and the value gradually decreases with increasing distance from the MTJ, transitioning toward a normal-faulting regime (Fig. 10a). The distance-dependent trend of A_ϕ values is more scattered but still discernible when considering all events instead of just background-seismicity (Fig. 10b). In contrast with the other study areas, the A_ϕ values of background and all seismicity in the NSAF show little dependence on distance from the MTJ (Fig. S9a).

4 DISCUSSION

The triple junction region in Cape Mendocino is characterized overall by a high level of background seismicity, low levels of clustered seismicity and aftershock productivity and diverse stress regimes. The analysis done in this work aims to clarify the relations between the intensity of background seismicity, earthquake clustering properties and the deviatoric stress field derived from stress inversions of the background and all earthquakes. For the GS and MTFZ regions, the aftershock productivity and intensity of background events tend to decrease with distance from the MTJ. In addition, the stress level is the most compressive ($A_\phi \approx 3$) at the MTJ and becomes less compressive with increasing distance from the junction. The concurrent spatial variation of the compressive stress level, aftershock productivity and intensity of background seismicity with distance from the MTJ suggests causal relations between these quantities. The positive correlation between the A_ϕ stress level and aftershock productivity implies that higher compressive stresses facilitate more regions to be closer to failure, and hence stress perturbations, such as those caused by co-seismic stress transfers, can result in more prominent aftershock sequences. Our results are consistent with inferences of previous studies that reported different types of clustering features in relation to the heat flow and the type of lithospheric deformation (I. Zaliapin & Y. Ben-Zion 2016b).

The highly compressional stress level observed in the MTJ is expected to result from the collision between the Gorda and the NAPs with a relative convergence rate of 32 mm yr^{–1} (R. McCaffrey *et al.* 2007; K.P. Furlong *et al.* 2024) and the crustal thickening of the overriding NAP (K.P. Furlong & R. Govers 1999; C.P. Nuyen & D.A. Schmidt 2022). The 1992 M_w 7.2 main shock occurred at the fault system with reverse kinematics, which extends directly through the MTJ (Figs 9 and 10). The decaying compressive stress level with increasing distance from the MTJ may explain the substantially higher aftershock productivity of the 1992 M_w 7.2 main shock than that of the 2024 M_w 7.0 main shock, even though their main shock magnitudes are similar (Fig. 5). The high stress levels near the MTJ may thus enhance the potential for earthquake triggering through remote events and other stress perturbations. This interpretation is

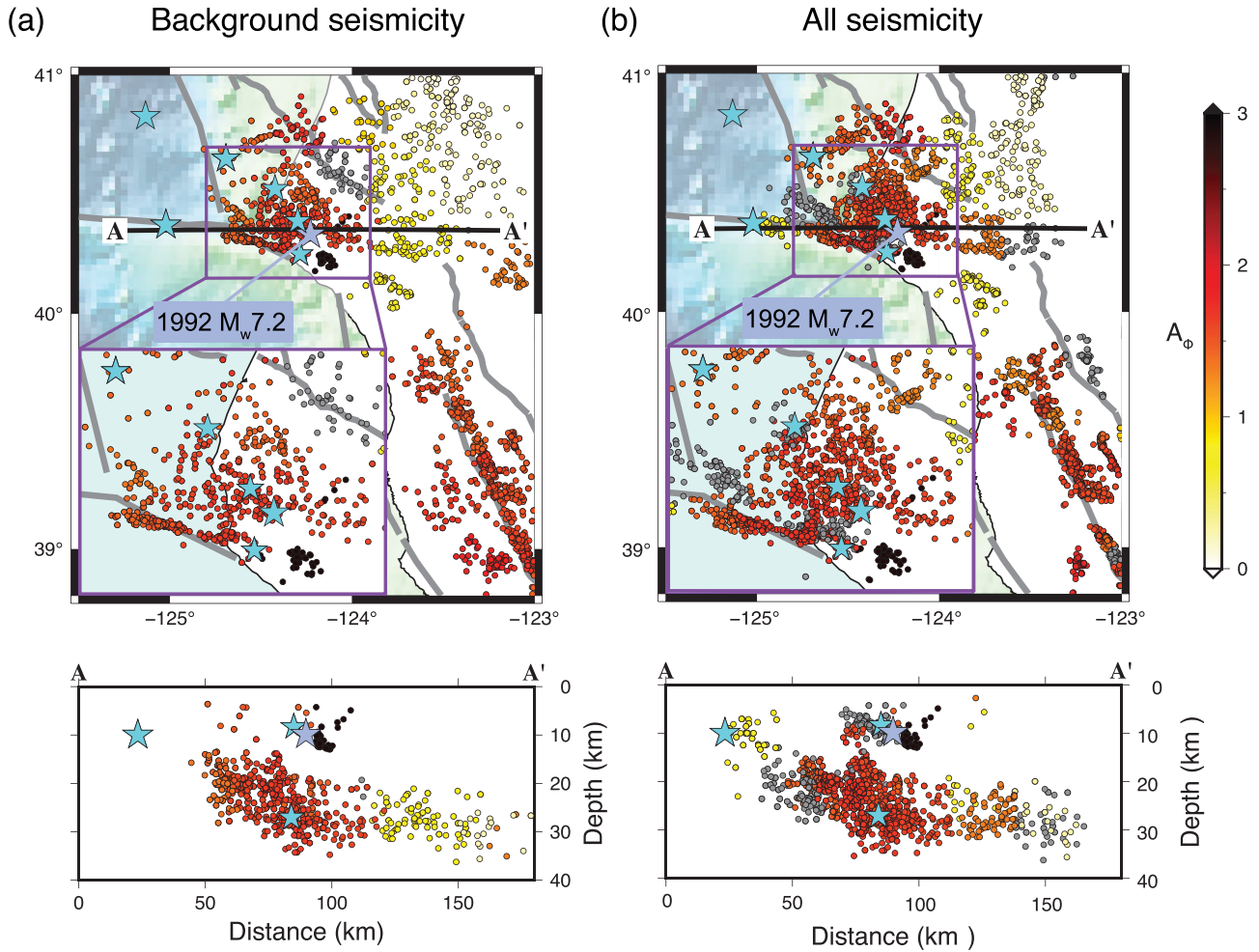


Figure 9. The A_ϕ value of each Voronoi cell in Cape Mendocino based on the inversion of (a) background seismicity and (b) all seismicity. The colour-bars are A_ϕ values. The thick and thin lines are faults and coastlines, respectively. The stars are $M_w \geq 6$ events between 1984 January 1 and 2025 January 31. The panels beneath the maps are the depth distribution of A_ϕ value in each Voronoi cell along profile A-A'.

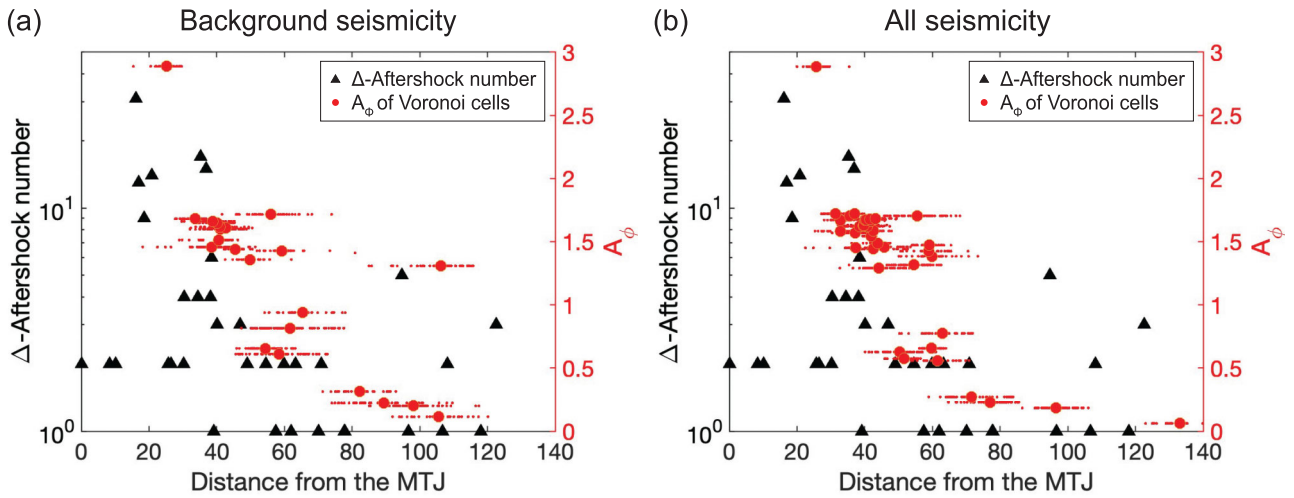


Figure 10. Relation between aftershock productivity of earthquake clusters ($\Delta = 2$), A_ϕ values of each Voronoi cell for (a) background seismicity and (b) all seismicity, and the distances of events to the MTJ in the MTFZ and GS. The triangles are the aftershock productivity of earthquake clusters. The dots are the distances of individual events in each Voronoi cell to the MTJ, while the circles are the average distances of each cell.

also consistent with the rapid dynamic triggering cases across diverse structures observed during the 1992 M_w 7.2 main shock and the 2021 Petrolia M_w 6 main shock (M.T. Hagerly & S.Y. Schwartz 1996; W.L. Yeck *et al.* 2023).

In addition to the stress level, aftershock productivity can also be affected by the temperature, rock types and lithospheric ages (Y. Ben-Zion & V. Lyakhovskiy 2006; K. Dascher-Cousineau *et al.* 2020; D.T. Trugman & Y. Ben-Zion 2023). Continental crust tends to exhibit higher aftershock productivity than oceanic crust; older, thicker and colder crust tends to have higher aftershock productivity than warmer, younger crust (I. Zaliapin & Y. Ben-Zion 2016b; K. Dascher-Cousineau *et al.* 2020). The MTJ region includes the thick, cold and brittle continental crust, which favours high aftershock productivity. In contrast, the younger age and warmer temperature of the oceanic crust closer to the Gorda ridge to the west, together with increasing depths to the subduction slab to the east, may reduce the aftershock productivity. The observed relations between aftershock productivity, intensity of background seismicity and distance from the MTJ may hold in other ridge–trench–fault triple junction regions. Future studies could expand our results and inferences framework to explore globally the correlations between distances from plate junctions, properties of aftershocks, background seismicity and stress parameters.

The NSAF has a stronger clustered mode in the nearest-neighbour diagram compared to the GS and MTFZ (Fig. 2d), but does not show correlation between seismicity and stress parameters (Fig. S9). This suggests that the background stress level may not be a significant factor affecting aftershock productivity in this region. The southern end of the MTJ beneath the NSAF forms a slab window, which separates the NSAF from the deforming slab and results in crustal extension (W.R. Dickinson & W.S. Snyder 1979; K.P. Furlong & R. Govers 1999). This separation might explain why the NSAF does not exhibit a decaying stress level from the MTJ (Fig. S9), as this region is less affected by slab-related compression. The consistent $S_{H_{\max}}$ orientations and dominant strike-slip faulting suggest that the NSAF experiences a strong and regionally coherent stress field driven by relative motion along the SAF and its subparallel fault systems. In addition, the seismicity in the NSAF has the highest foreshock fraction but the lowest aftershock fraction compared to the other two regions (Fig. 4). A possible explanation is that the upwelling asthenosphere through the slab window increases the surface heat flow (C.A. Guzofski & K.P. Furlong 2002; K.P. Furlong *et al.* 2024), which may reduce lithospheric strength, enhance aseismic processes and could in turn lead to increased foreshock activity in the NSAF (K.P. Furlong *et al.* 1989; X. Chen & P.M. Shearer 2013). The relation between a higher proportion of foreshocks and higher heat flow is consistent with the observations in previous studies (e.g. I. Zaliapin & Y. Ben-Zion 2013b; 2016b; D.T. Trugman & Z.E. Ross 2019; P. Martínez-Garzón *et al.* 2019).

The tectonic and seismic characteristics in the GS reveal a complex interplay between stress and strain. The discrepancy between the $S_{H_{\max}}$ orientation in the GS and the most compressive horizontal strain in the overriding NAP (Fig. S7) may indicate a decoupling between these two plates and a low-friction subduction interface (K. Wang 2000; D. Li *et al.* 2018). This may result from enhanced fluid pressure during the hydration process, which may be driven by internal slab deformation associated with bending and subduction-related extension (D.R. Shelly *et al.* 2024). These deformation processes contribute to a considerable normal faulting fraction compared to other focal mechanism types in the GS, even though it is located within the subduction zone (Fig. 7).

The faulting styles between background and clustered seismicity in the MTFZ and NSAF are generally consistent. This consistency indicates that the stress perturbations resulting from aftershock sequences may not significantly alter the regional stress field. Notably, the GS exhibits a transition in faulting types within clustered events. In a normal faulting regime, if the magnitude of the vertical stress (S_v) decreases below $S_{H_{\max}}$ or if $S_{H_{\max}}$ exceeds S_v , the stress regime will change from normal to strike-slip faulting. Thus, the reduction of normal faulting but increasing strike-slip faulting observed in clustered seismicity within the GS may reflect shallower earthquake depths or enhanced north–south $S_{H_{\max}}$, which may be driven by stress redistribution of aftershock sequences. Overall, these findings highlight the importance of considering both slab-internal deformation processes and overriding plate dynamics when interpreting seismicity characteristics in the GS.

5 CONCLUSIONS

Our results reveal systematic spatial variations in seismicity and stress parameters within the MTFZ and the GS as a function of distance from the MTJ, which is here represented by the hypocentre of the 1992 M_w 7.2 earthquake. Both the aftershock productivity and the A_ϕ value tend to decrease with increasing distance from the MTJ. Similarly, the background earthquake intensity in both the MTFZ and GS tends to decrease with distance from the MTJ.

Compared to the MTFZ and GS, the NSAF region exhibits a higher proportion of foreshocks and more swarm-like clusters, which may be associated with increased surface heat flow and aseismic failure processes. In the GS, most earthquakes exhibit focal mechanisms of strike-slip or normal faulting despite the overall subduction setting. The abundant normal faulting mechanisms may be associated with the flat-angle subduction of the slab, which can generate extensional stresses due to horizontal drag. The abundance of strike-slip mechanisms likely reflects the reactivation of pre-existing normal faults under north–south $S_{H_{\max}}$ orientation of the GS. Furthermore, the high proportion of normal faulting in background seismicity potentially indicates internal slab bending.

These observations provide new insights into how tectonic processes and their resulting stress field control the characteristics and spatial distribution of seismicity near the MTJ, especially the systematic decay of aftershock productivity, intensity of background seismicity and the stress level with increasing distance from the MTJ. Our results contribute to a better understanding of the mechanical processes and seismicity in the Cape Mendocino region.

DATA AVAILABILITY

Data products for this study were accessed through C.P. NCEDC (2014). The F. Waldhauser & D.P. Schaff (2008) catalogues used in the study are from C.P. NCEDC (2014). The earthquake cluster detection and catalogue declustering algorithms were developed by Zaliapin and Ben-Zion (2013a, , 2020). The codes are available at https://github.com/dttrugman/Nearest_Neighbor_Cluster and https://github.com/dttrugman/Nearest_Neighbor_Declustering. The MSATSI software was developed by P. Martínez-Garzón *et al.* (2014). The software is available at <https://www.gfz.de/en/section/geomechanics-and-scientific-drilling/data-products-services/msatsi>. The original algorithm is based on the SATSI C-library by J.L. Hardebeck & A.J. Michael (2006). We thank the two anonymous referees for useful comments that helped us to improve the manuscript.

ACKNOWLEDGMENTS

The research was supported by the Statewide California Earthquake Center (based on NSF Cooperative Agreement EAR-2225216 and USGS Cooperative Agreement G24AC00072-00) and NSF Award EAR-2121666. PMG acknowledges funding from the ERC Starting Grant -101076119 (QUAKEHUNTER).

SUPPORTING INFORMATION

Supplementary data are available at [GJIRAS](https://doi.org/10.1093/gji/ggab089) online.

Figure S1. Relation between Δ -aftershock number of the earthquake clusters in the MTFZ and GS, and their main shock distances to the MTJ based on the parameters of (a) $\Delta = 2$, (b) $\Delta = 3$ and (c) $\Delta = 3.5$. The stars are $M \geq 6$ events. The MTJ location is defined as the hypocentre of the 1992 M_w 7.2 main shock.

Figure S2. (a) Tectonic setting in Cape Mendocino together with instrumental seismicity with $M \geq 2.5$ between 1984 January 1 and 2025 January 31. The dots represent the seismic events in the Mendocino Transform Fault Zone (MTFZ), the Gorda Slab (GS), the North American Plate (NAP), and the Northern San Andreas Fault system (NSAF). The location of the Mendocino Triple Junction (MTJ) is defined as the hypocentre of the 1992 M_w 7.2 main shock. The abbreviation of GR is Gorda Ridge. Arrows indicate the sense of plate motion. The thick and thin lines are faults and coastlines. (b) Depth distribution of events along the A-A' profile. The stars in (a) and (b) mark $M_w \geq 6$ earthquakes. Events located within ~ 15 km from the profile line are projected onto the profile. (c) Depth distribution of events along the B-B' profile.

Figure S3. The joint distribution of rescaled time (T) and space (R) components of the nearest-neighbour proximity (eq. 2) of $M_p \geq 2.5$ events from 1984 January 1 to 2025 January 31 in the F. Waldhauser & D.P. Schaff (2008) catalogue in (a) the whole study area, (b) MTFZ, (c) NAP, (d) GS and (e) NSAF. The black line in (a) is $\log T + \log R = -4.03$. The colourbar is the kernel density of the event distribution.

Figure S4. The proportion of aftershocks, main shocks, and foreshocks in the MTFZ, GS, NAP and NSAF.

Figure S5. Relation between Δ -foreshock number of the earthquake clusters in the MTFZ and GS, and their main shock distances to the MTJ based on the parameters of $\Delta = 2$. The MTJ location is defined as the hypocentre of the 1992 M_w 7.2 main shock.

Figure S6. Proportion of focal mechanism types of (a) background and (b) clustered seismicity in the GS, MTFZ, NAP and NSAF. The bars represent the normal, reverse and strike-slip faulting, respectively.

Figure S7. S_{HMax} and strain rate orientations in Cape Mendocino. The S_{HMax} symbol and stress regime classification are provided in the legend. The bars are the azimuth of the most compressive principal strain rate from C.P. Nuyen & D.A. Schmidt (2022) and C.P. Nuyen (2022), under the terms of the CC BY 4.0 license (<https://creativecommons.org/licenses/by/4.0/>). The thick and thin lines are faults and coastlines. The stars are $M \geq 6$ events during the analysed time period.

Figure S8. S_{HMax} orientations of each Voronoi cell in Cape Mendocino based on the inversion of (a and b) background and (c and d) all seismicity. In (a) and (c), the thick and thin lines are faults and coastlines. The stars are $M_w \geq 6$ events between 1984 January 1 and 2025 January 31. The panels beneath the maps are the depth distribution of fault types in each Voronoi cell along profile A-A'. The S_{HMax} symbol and stress regime classification are provided in the legend. (b and d) Stereonets based on the inversion of background and all seismicity in the GS, MTFZ, NAP and NSAF. The orientations of three principal stresses σ_1 , σ_2 and σ_3 are indicated in the plot, represented by the 95 per cent confidence interval from bootstrap resampling. The best orientation of each principal stress axis is given with a cross.

Figure S9. Relation between aftershock productivity of earthquake clusters ($\Delta = 1.5$), A_ϕ values of each Voronoi cell for (a) background seismicity and (b) all seismicity, and the distances of events to the MTJ in the NSAF. The triangles are the aftershock productivity of earthquake clusters. The dots are the distances of individual events in each Voronoi cell to the MTJ, while the circles are the average distances of each cell.

Please note: Oxford University Press is not responsible for the content or functionality of any supporting materials supplied by the authors. Any queries (other than missing material) should be directed to the corresponding author for the paper.

REFERENCES

- Abolfathian, N., Martínez-Garzón, P. & Ben-Zion, Y., 2018. Spatiotemporal variations of stress and strain parameters in the San Jacinto Fault Zone, *Pure appl. Geophys.*, **176**, 1145–1168.
- Atterholt, J., McGuire, J.J., Barbour, A.J., Stewart, C. & Moschetti, M.P., 2025. Fiber-imaged supershear dynamics in the 2024 M_w 7 Mendocino Fault earthquake, *Science*, **389**(6767), 1361–1365.
- Baiesi, M. & Paczuski, M., 2004. Scale-free networks of earthquakes and aftershocks, *Phys. Rev. E*, **69**, 066106.
- Ben-Zion, Y., 2001. On quantification of the earthquake source, *Seismol. Res. Lett.*, **72**, 151–152.
- Ben-Zion, Y., 2008. Collective behavior of earthquakes and faults: continuum–discrete transitions, progressive evolutionary changes, and different dynamic regimes, *Rev. Geophys.*, **46**(4), e2008RG000260.
- Ben-Zion, Y. & Lyakhovskiy, V., 2006. Analysis of aftershocks in a lithospheric model with seismogenic zone governed by damage rheology, *Geophys. J. Int.*, **165**(1), 197–210.
- Bott, M.H., 1959. The mechanics of oblique slip faulting, *Geol. Mag.*, **96**, 109–117.
- Chen, X. & Shearer, P.M., 2013. California foreshock sequences suggest aseismic triggering process, *Geophys. J. Int.*, **40**(11), 2602–2607.
- Dascher-Cousineau, K., Brodsky, E.E., Lay, T. & Goebel, T., 2020. What controls variations in aftershock productivity?, *J. geophys. Res.: Solid Earth*, **125**, e2019JB018111.
- Dickinson, W.R. & Snyder, W.S., 1979. Geometry of subducted slabs related to San Andreas transform, *J. Geol.*, **87**(6), 609–627.
- Fitch, T.J., 1972. Plate convergence, transcurrent faults and internal deformation adjacent to Southeast Asia and the western Pacific, *J. geophys. Res.*, **77**, 4432–4460.
- Furlong, K.P. & Govers, R., 1999. Ephemeral crustal thickening at a triple junction: the Mendocino crustal conveyor, *Geology*, **27**(2), 127–130.
- Furlong, K.P., Hugo, W.D. & Zandt, G., 1989. Geometry and evolution of the San Andreas Fault Zone in northern California, *J. geophys. Res.*, **94**(B3), 3100–3110.
- Furlong, K.P., Villaseñor, A., Benz, H.M. & McKenzie, K.A., 2024. Formation and evolution of the Pacific–North American (San Andreas) plate boundary: constraints from the crustal architecture of Northern California, *Tectonics*, **43**(6), e2023TC007963.
- Gentili, S., Peresan, A., Talebi, M., Zare, M. & Di Giovambattista, R., 2019. A seismic quiescence before the 2017 M_w 7.3 Sarpol Zahab (Iran) earthquake: detection and analysis by improved RTLmethod, *Phys. Earth planet. Inter.*, **290**, 10–19.
- Goebel, T.H., Rosson, Z., Brodsky, E.E. & Walter, J.I. 2019. Aftershock deficiency of induced earthquake sequences during rapid mitigation efforts in Oklahoma, *Earth planet. Sci. Lett.*, **522**, 135–143.
- Gulick, S.P., Meltzer, A.S., Henstock, T.J. & Levander, A., 2001. Internal deformation of the southern Gorda plate: fragmentation of a weak plate near the Mendocino triple junction, *Geology*, **29**(8), 691–694.
- Guo, H., McGuire, J.J. & Zhang, H., 2021. Correlation of porosity variations and rheological transitions on the southern Cascadia megathrust, *Nature Geosci.*, **14**(5), 341–348.
- Guzowski, C.A. & Furlong, K.P., 2002. Migration of the Mendocino triple junction and ephemeral crustal deformation: implications for California Coast Range heat flow, *Geophys. Res. Lett.*, **29**(1), 12–11.
- Hagerty, M.T. & Schwartz, S.Y., 1996. The 1992 Cape Mendocino earthquake: broadband determination of source parameters, *J. geophys. Res.: Solid Earth*, **101**(B7), 16 043–16 058.
- Hardebeck, J.L. & Hauksson, E., 1999. Role of fluids in faulting inferred from stress field signatures, *Science*, **285**(5425), 236–239.
- Hardebeck, J.L., Llenos, A.L., Michael, A.J., Page, M.T. & Van Der Elst, N., 2019. Updated California aftershock parameters, *Seismol. Res. Lett.*, **90**(1), 262–270.
- Hardebeck, J.L. & Michael, A.J., 2004. Stress orientations at intermediate angles to the San Andreas Fault, California, *J. geophys. Res.: Solid Earth*, **109**(B11), e2004JB003239.
- Hardebeck, J.L. & Michael, A.J., 2006. Damped regional-scale stress inversions: methodology and examples for southern California and the Coalinga aftershock sequence, *J. geophys. Res.: Solid Earth*, **111**(B11), e2005JB004144.
- Hartigan, J.A. & Wong, M.A., 1979. Algorithm AS 136: a k-means clustering algorithm, *J. R. Stat. Soc. C Appl. Stat.*, **28**(1), 100–108.
- Hellweg, M., Dreger, D.S., Lomax, A., McPherson, R.C. & Dengler, L., 2025. The 2021 and 2022 North Coast California earthquake sequences and fault complexity in the vicinity of the Mendocino triple junction, *Bull. seism. Soc. Am.*, **115**(1), 140–162.
- Hsu, Y.F., Zaliapin, I. & Ben-Zion, Y., 2024. Informative modes of seismicity in nearest-neighbor earthquake proximities, *J. geophys. Res.: Solid Earth*, **129**(3), e2023JB027826.
- Karimi, K. & Davidsen, J., 2023. Separating primary and secondary mechanisms for seismicity induced by hydraulic fracturing, *Bull. seism. Soc. Am.*, **113**(5), 1982–1991.
- Li, D., McGuire, J.J., Liu, Y. & Hardebeck, J.L., 2018. Stress rotation across the Cascadia megathrust requires a weak subduction plate boundary at seismogenic depths, *Earth planet. Sci. Lett.*, **485**, 55–64.
- Lund, B. & Townend, J., 2007. Calculating horizontal stress orientations with full or partial knowledge of the tectonic stress tensor, *Geophys. J. Int.*, **170**(3), 1328–1335.
- Lundstern, J.E., 2024. *Recent advances in characterizing the crustal stress field and future applications of stress data: perspectives from North America*, Geological Society of London. doi:
- Martínez-Garzón, P., Ben-Zion, Y., Abolfathian, N., Kwiatek, G. & Bohnhoff, M., 2016. A refined methodology for stress inversions of earthquake focal mechanisms, *J. geophys. Res.: Solid Earth*, **121**(12), 8666–8687.
- Martínez-Garzón, P., Ben-Zion, Y., Zaliapin, I. & Bohnhoff, M., 2019. Seismic clustering in the Sea of Marmara: implications for monitoring earthquake processes, *Tectonophysics*, **768**, 228176.
- Martínez-Garzón, P., Kwiatek, G., Ickrath, M. & Bohnhoff, M., 2014. MSATSI: a MATLAB package for stress inversion combining solid classic methodology, a new simplified user-handling, and a visualization tool, *Seismol. Res. Lett.*, **85**(4), 896–904.
- Martínez-Garzón, P., Zaliapin, I., Ben-Zion, Y., Kwiatek, G. & Bohnhoff, M., 2018. Comparative study of earthquake clustering in relation to hydraulic activities at geothermal fields in California, *J. geophys. Res.: Solid Earth*, **123**(5), 4041–4062.
- Materna, K., Taira, T.A. & Bürgmann, R., 2018. Aseismic transform fault slip at the Mendocino Triple Junction from characteristically repeating earthquakes, *Geophys. Res. Lett.*, **45**(2), 699–707.
- McCaffrey, R. et al. 2007. Fault locking, block rotation and crustal deformation in the Pacific Northwest, *Geophys. J. Int.*, **169**(3), 1315–1340.

- McGuire, J.J., Boettcher, M.S. & Jordan, T.H., 2005. Foreshock sequences and short-term earthquake predictability on East Pacific Rise transform faults, *Nature*, **434**(7032), 457–461.
- Michael, A.J., 1987. Use of focal mechanisms to determine stress: a control study, *J. geophys. Res.: Solid Earth*, **92**(B1), 357–368.
- NCEDC, 2014. *Northern California Earthquake Data Center*. UC Berkeley Seismological Laboratory. Dataset.
- Nuyen, C.P., 2022. Strain rate results and block modeling files for Southern Cascadia, in *Mendeley Data*, Ver. 1. Available at: <https://data.mendeley.com/datasets/xfr8sprcf5/1>.
- Nuyen, C.P. & Schmidt, D.A., 2022. Strain partitioning among forearc faults in southern Cascadia inferred from GNSS, *J. geophys. Res.: Solid Earth*, **127**(8), e2022JB024236.
- Oppenheimer, D. et al., 1993. The Cape Mendocino, California, earthquakes of April 1992: subduction at the triple junction, *Science*, **261**(5120), 433–438.
- Pollitz, F.F., Guns, K.A. & Yoon, C.E., 2025. Rupture process of the Mw7.0 December 5, 2024 Offshore Cape Mendocino Earthquake, *Geophys. Res. Lett.*, **52**(14), e2025GL115613.
- Reasenber, P. & Oppenheimer, D., 1986. *FPPFIT, FPLOT and FPPAGE: Fortran computer programs for calculating and displaying earthquake fault-plane solutions*, Vol. 85, US Geol. Surv. Available at: <https://www.usgs.gov/software/fpfit-fpplot-and-fppage>.
- Riddihough, R., 1984. Recent movements of the Juan de Fuca plate system, *J. geophys. Res.: Solid Earth*, **89**(B8), 6980–6994.
- Sammis, C., King, G. & Biegel, R., 1987. The kinematics of gouge deformation, *Pure appl. Geophys.*, **125**, 777–812.
- Shakibay Senobari, N. & Funning, G.J., 2019. Widespread fault creep in the northern San Francisco Bay Area revealed by multistation cluster detection of repeating earthquakes, *Geophys. Res. Lett.*, **46**(12), 6425–6434.
- Shelly, D.R. et al., 2024. Subduction intraslab-interface fault interactions in the 2022 M_w 6.4 Ferndale, California, earthquake sequence, *Sci. Adv.*, **10**, ead11226.
- Simpson, R.W., 1997. Quantifying Anderson's fault types, *J. geophys. Res.: Solid Earth*, **102**(B8), 17 909–17 919.
- Townend, J. & Zoback, M.D., 2001. Implications of earthquake focal mechanisms for the frictional strength of the San Andreas fault system, in *The Nature and Tectonic Significance of Fault Zone Weakening*, eds Holdsworth, R.E., Strachan, R.A., Magloughlin, J.F. & Knipe, R.J., Geological Society of London. doi:
- Trugman, D.T. & Ben-Zion, Y., 2023. Coherent spatial variations in the productivity of earthquake sequences in California and Nevada, *Seismol. Rec.*, **3**(4), 322–331.
- Trugman, D.T. & Ben-Zion, Y., 2024. Potency–Magnitude scaling relations and a unified earthquake catalog for the western United States, *Seismol. Rec.*, **4**(3), 223–230.
- Trugman, D.T. & Ross, Z.E., 2019. Pervasive foreshock activity across southern California, *Geophys. Res. Lett.*, **46**(15), 8772–8781.
- Vavryčuk, V., 2011. Principal earthquakes: theory and observations for the 2008 West Bohemia swarm, *Earth planet. Sci. Lett.*, **305**(3–4), 290–296.
- Vavryčuk, V., 2014. Iterative joint inversion for stress and fault orientations from focal mechanisms, *Geophys. J. Int.*, **199**(1), 69–77.
- Vavryčuk, V., Bouchaala, F. & Fischer, T., 2013. High-resolution fault image from accurate locations and focal mechanisms of the 2008 swarm earthquakes in West Bohemia, Czech Republic, *Tectonophysics*, **590**, 189–195.
- Voronoi, G., 1908. Nouvelles applications des paramètres continus à la théorie de formes quadratiques, *J. Reine Angew. Math.*, **134**, 198–287.
- Waldhauser, F., 2001. *HypoDD-A Program to Compute Double-difference Hypocenter Locations*, No. 2001-113, USGS
- Waldhauser, F. & Ellsworth, W.L., 2000. A double-difference earthquake location algorithm: method and application to the northern Hayward fault, California, *Bull. seism. Soc. Am.*, **90**(6), 1353–1368.
- Waldhauser, F. & Schaff, D.P., 2008. Large-scale relocation of two decades of Northern California seismicity using cross-correlation and double-difference methods, *J. geophys. Res.: Solid Earth*, **113**(B8), e2007JB005479
- Waldhauser, F. & Schaff, D.P., 2021. A comprehensive search for repeating earthquakes in northern California: implications for fault creep, slip rates, slip partitioning, and transient stress, *J. geophys. Res.: Solid Earth*, **126**(11), e2021JB022495.
- Wallace, R.E., 1951. Geometry of shearing stress and relation to faulting, *J. Geol.*, **59**(2), 118–130.
- Wang, K., 2000. Stress–strain ‘paradox’, plate coupling, and forearc seismicity at the Cascadia and Nankai subduction zones, *Tectonophysics*, **319**(4), 321–338.
- Yeck, W.L., Shelly, D.R., Materna, K.Z., Goldberg, D.E. & Earle, P.S., 2023. Dense geophysical observations reveal a triggered, concurrent multi-fault rupture at the Mendocino Triple Junction, *Commun. Earth Environ.*, **4**(1), 94.
- Yoon, C.E. & Shelly, D.R., 2024. Distinct yet adjacent earthquake sequences near the Mendocino Triple Junction: 20 December 2021 M_w 6.1 and 6.0 Petrolia, and 20 December 2022 M_w 6.4 Ferndale, *The Seismic Record*, **4**(1), 81–92.
- Zaliapin, I. & Ben-Zion, Y., 2013a. Earthquake clusters in southern California I: identification and stability, *J. geophys. Res.: Solid Earth*, **118**(6), 2847–2864.
- Zaliapin, I. & Ben-Zion, Y., 2013b. Earthquake clusters in southern California II: classification and relation to physical properties of the crust, *J. geophys. Res.: Solid Earth*, **118**(6), 2865–2877.
- Zaliapin, I. & Ben-Zion, Y., 2015. Artefacts of earthquake location errors and short-term incompleteness on seismicity clusters in southern California, *Geophys. J. Int.*, **202**(3), 1949–1968.
- Zaliapin, I. & Ben-Zion, Y., 2016a. Discriminating characteristics of tectonic and human-induced seismicity, *Bull. seism. Soc. Am.*, **106**(3), 846–859.
- Zaliapin, I. & Ben-Zion, Y., 2016b. A global classification and characterization of earthquake clusters, *Geophys. J. Int.*, **207**(1), 608–634.
- Zaliapin, I. & Ben-Zion, Y., 2020. Earthquake declustering using the nearest-neighbor approach in space-time-magnitude domain, *J. geophys. Res.: Solid Earth*, **125**(4), e2018JB017120.
- Zaliapin, I. & Ben-Zion, Y., 2022. Perspectives on clustering and declustering of earthquakes, *Seismol. Res. Lett.*, **93**, 386–401.
- Zoback, M.L., 1992. First- and second-order patterns of stress in the lithosphere: the World Stress Map Project, *J. geophys. Res.: Solid Earth*, **97**(B8), 11 703–11 728.